



ELSEVIER

Contents lists available at ScienceDirect

Acta Biomaterialia

journal homepage: www.elsevier.com/locate/actbio

Full length article

3D microengineered vascularized tumor spheroids for drug delivery and efficacy testing[☆]

Jungho Ahn^{a,b,1}, Da-Hyun Kim^{c,1}, Dong-Jun Koo^{d,e,1}, Jungeun Lim^a, Tae-Eun Park^f,
Jungseub Lee^a, Jihoon Ko^a, Seongchan Kim^g, Minjae Kim^g, Kyung-Sun Kang^c,
Dal-Hee Min^g, Sung-Yon Kim^{d,e,g,*}, YongTae Kim^{b,h,i,j,*}, Noo Li Jeon^{a,k,l,*}

^a Department of Mechanical and Aerospace Engineering, Seoul National University, Seoul 08826, Republic of Korea

^b George W. Woodruff School of Mechanical Engineering, Georgia Institute of Technology, Atlanta, GA 30332, USA

^c Adult Stem Cell Research Center and Research Institute for Veterinary Science, College of Veterinary Medicine, Seoul National University, Seoul 08826, Republic of Korea

^d Institute of Molecular Biology and Genetics, Seoul National University, Seoul 08826, South Korea

^e Program in Neuroscience, Seoul National University, Seoul 08826, South Korea

^f Ulsan National Institute of Science and Technology, Ulsan 44914, Republic of Korea

^g Department of Chemistry, Seoul National University, Seoul 08826, Republic of Korea

^h Parker H. Petit Institute for Bioengineering and Bioscience, Georgia Institute of Technology, Atlanta, GA 30332, USA

ⁱ Institute for Electronics and Nanotechnology, Georgia Institute of Technology, Atlanta, GA 30332, USA

^j Wallace H. Coulter Department of Biomedical Engineering, Georgia Institute of Technology, Atlanta, GA 30332, USA

^k Division of WCU (World Class University) Multiscale Mechanical Design, Seoul National University, Seoul 08826, Republic of Korea

^l Seoul National University Institute of Advanced Machines and Design, Seoul 08826, Republic of Korea

ARTICLE INFO

Article history:

Received 6 June 2022

Revised 3 October 2022

Accepted 4 October 2022

Available online xxx

Keywords:

Microfluidics

Organ-on-a-chip

Tumor microenvironment

Tumor angiogenesis

Drug screening

Vascularized tumor

Leaky tumor vasculature

ABSTRACT

Tumor angiogenesis is regarded as a promising target for limiting cancer progression because tumor-associated vasculature supplies blood and provides a path for metastasis. Thus, *in vitro* recapitulation of vascularized tumors is critical to understand the pathology of cancer and identify the mechanisms by which tumor cells proliferate, metastasize, and respond to drugs. In this study, we microengineered a vascularized tumor spheroid (VTS) model to reproduce the pathological features of solid tumors. We first generated tumor-EC hybrid spheroids with self-assembled intratumoral vessels, which enhanced the uniformity of the spheroids and peritumoral angiogenic capacity compared to spheroids composed only with cancer cells. Notably, the hybrid spheroids also exhibited expression profiles associated with aggressive behavior. The blood vessels sprouting around the hybrid spheroids on the VTS chip displayed the distinctive characteristics of leaky tumor vessels. With the VTS chip showing a progressive tumor phenotype, we validated the suppressive effects of axitinib on tumor growth and angiogenesis, which depended on exposure dose and time, highlighting the significance of tumor vascularization to predict the efficacy of anticancer drugs. Ultimately, we effectively induced both lymphangiogenesis and angiogenesis around the tumor spheroid by promoting interstitial flow. Thus, our VTS model is a valuable platform with which to investigate the interactions between tumor microenvironments and explore therapeutic strategies in cancer.

Statement of significance

We conducted an integrative study within a vascularized tumor spheroid (VTS) model. We first generated tumor-EC hybrid spheroids with self-assembled intratumoral vessels, which enhanced the uniformity of the spheroids and peritumoral angiogenic capacity compared to spheroids composed only with cancer cells. Through RNA sequencing, we elucidated that the tumor-EC hybrid spheroids exhibited ex-

[☆] Part of the Special Issue on Biofabrication with Spheroid and Organoid Materials, guest-edited by Professors Mark Skylar-Scott, Heidi Declercq, and Koichi Nakayama.

* Corresponding authors.

E-mail addresses: sungyonkim@snu.ac.kr (S.-Y. Kim), ytkim@gatech.edu (Y. Kim), njeon@snu.ac.kr (N.L. Jeon).

¹ These authors contributed equally to this work.

pression profiles associated with aggressive behavior such as cancer progression, invasion and metastasis. The blood vessels sprouting around the hybrid spheroids on the VTS chip displayed the distinctive characteristics of leaky tumor vessels. We further validated the suppressive effects of axitinib on tumor growth and angiogenesis, depending on exposure dose and time. Ultimately, we effectively induced both lymphangiogenesis and angiogenesis around the tumor spheroid by promoting interstitial flow.

© 2022 Published by Elsevier Ltd on behalf of Acta Materialia Inc.

1. Introduction

The tumor microenvironment (TME) is regarded as a critical feature of tumors because it participates in cancer development and progression [1]. It comprises a milieu of various cells (e.g., surrounding blood vessel cells, fibroblasts, immune cells and cancer stem cells) and even noncellular components (e.g., the extracellular matrix (ECM)) [2–4]. The interplay among various components within the TME induces growth signaling, intermediate metabolite production, and promotes a favorable environment for tumor cells to proliferate and metastasize [1]. Hence, simplified conventional models consisting of a homogeneous collection of neoplastic cells have been found to be insufficient to properly reflect cancer biology [5]. Moreover, the complex interactions within the TME need to be thoroughly investigated to develop anticancer strategies [6]. Nevertheless, most *in vitro* studies use two-dimensional (2D) tumor cell cultures with no consideration of the TME, making them unsuitable to study the effects of the complex spatial organization and interaction of tumor-associated cells [7].

While xenograft animal models of cancer can provide essential *in vivo* characteristics of tumor growth and responses to drug molecules, it remains extremely difficult to accurately mimic the process of human tumorigenesis due to species discrepancies and limited mechanistic approaches of animal models [8]. This challenge highlights the importance of using realistic TME modeling *in vitro*. Recent advances in engineered TMEs using multicellular organ-on-a-chip technology have enabled the development of pathologically and physiologically relevant human models of tumorigenic processes. Especially, metastasis-on-a-chip which recapitulates a broad spectrum of cancer cell invasion and migration (e.g., cancer intravasation and extravasation) that occurs in TME have been proposed [9–11]. In addition, angiogenic sprouting which is induced by single tumor cells or tumor spheroid into 3D hydrogel models has been developed in 3D microfluidic systems [12–14]. Since the cancer associated fibroblasts play a crucial role in the heterogeneity and plasticity in the TME, several studies have been conducted recently [15,16]. For instance, tissue specific decellularized extracellular matrices have been used to reconstitute highly biomimetic TME in a chip level [17]. More recently, investigating the effect of immune cells on the inception of collective 3D invasion of tumor cells in tumor-immune microenvironment on-a-chip has been reported [18,19]. High-content and high-throughput models made of PDMS (Polydimethylsiloxane) or injection-molded polystyrene have been introduced for robust and efficient screening of drug candidates [20–22].

To engineer the TME on a chip, multicellular tumor spheroids have been widely used to mimic solid tumors [23,24]. Tumor spheroids are compact heterogeneous cellular aggregates that are assembled with multiple cell types (e.g., epithelial, mesenchymal, and endothelial cells). In contrast to that of 2D cultured cell cultures, the microenvironment of multicellular spheroid cultures is created in three dimensions, which allows the formation of a nutrient/oxygen gradient within the spheroids and cell–cell/cell–ECM interactions [25–27]. In particular, the interactions between cancer cells and endothelial cells (ECs) have been extensively investigated [28–30]. Since tumor growth and metastasis are extensively

affected by the tumor vasculature [31], tumor angiogenesis is a valid therapeutic target for many solid tumors, particularly in the context of cancer progression and metastasis [32]. In this regard, multicellular spheroids connected with vessel-like tubular structures have been usefully employed for evaluating drug responses [27,33–35].

In this study, we presented an integrative study of a vascularized tumor spheroid (VTS) chip in which multicellular cancer spheroids were incorporated with a 3D perfusable vascular bed. We first generated tumor-EC hybrid spheroids exhibiting aggressive behavior, such as cancer progression and invasion. Then, we demonstrated key pathologic features of vascularized tumors, such as proangiogenic behavior of tumors and leaky tumor-associated vasculature in VTS chips. Furthermore, we successfully presented a complicated TME including both lymphatic and blood vessels within the VTS chip through interstitial flow stimulation. To confirm the usefulness of our VTS chip as a drug screening platform, the responses of both the spheroids and vasculature were analyzed after exposing the VTS chip to axitinib. Taken together, our findings showed that our VTS model closely recapitulated various characteristics of vascularized solid tumors, representing a promising *in vitro* platform for preclinical experimentation.

2. Materials and methods

2.1. Cell culture and spheroid formation

Human umbilical vein endothelial cells (HUVECs, Lonza, Switzerland) were cultured in Endothelial Growth Medium (EGM-2, Lonza) and passage 4 was used for the experiments. Red fluorescent protein (RFP) expressing HUVECs were obtained from Anigio-Proteomie (Boston, MA, USA). Human dermal lymphatic endothelial cells (LECs, HMVEC-dly, Lonza) were cultured in EGM-2 supplemented with EGM-2 MV BulletKit and passages 6–7 used for experiments. LECs were used for experiments before reaching confluence (80–90%). Normal human lung fibroblasts (LFs, Lonza) were cultured in Fibroblast Growth Medium (FGM-2, Lonza) and passage 6 was used for the experiments. Human hepatocellular carcinoma cells (HepG2, Korean Cell Line Bank) were cultured in DMEM supplemented with 10% FBS, penicillin (100 U/mL) and streptomycin (100 U/mL). All cells were maintained in a humidified incubator at 37 °C and 5% CO₂. In this study, we prepared 3 types of spheroids: a HepG2 only spheroid and hybrid spheroid composed of HepG2 cells and HUVEC with different ratios (4:1 and 1:1) (Supplementary Fig. S1). They were grown in a 96-well plate with U-shaped bottom wells (Sumitomo Bakelite, Tokyo, Japan). For suspension culture, EGM-2 medium was used for the cancer monoculture spheroid and the co-culture spheroid. All cell suspensions were prepared for a total of 5000 cells and mixed with 1% volume ratio of Matrigel in 200 μL of medium. After pre-culturing in a 96-well plate, a spheroid was introduced into the spheroid culture device. We used 4 to 6 days cultured spheroid for the experiments.

2.2. Fabrication of the microfluidic device

The microfluidic device was fabricated with PDMS (polydimethylsiloxane, Sylgard 184, Dow Corning, USA) using soft lithog-

raphy and replica molding. The microfluidic device was modified from a previously reported device from our group. The channels were separated by micro-posts with 150 μm heights and 100 μm intervals. Slide cover glass (50 mm \times 70 mm, Matsunami, Bellingham, WA, USA) and PDMS were covalently bonded to each other by air plasma treatment (Fetmo Science, Republic of Korea). The 120 μm thick structure was patterned on the silicon wafer by photolithography with SU-8 150 photoresist (MicroChem). The PDMS base mixed with a curing agent at a ratio of 10:1 (w/w) was poured on the silicon wafer and cured for 3 h on a 90 °C hotplate. PDMS was detached from the wafer when fully solidified. Using biopsy punch 1 and 6 mm, cell injection ports and reservoirs for culture media were punched out. Gel injection port also punched out by biopsy punch 1mm; used for loading cancer spheroid and medium. After bonded, the device was stored in an 80 °C dry oven for 3 days to be completely cured and to make its surface hydrophobic.

2.3. Cell seeding in the microfluidic platform

A tumor spheroid was collected from a 96-well plate using a 200 μL pipette tip and mixed with HUVECs suspension in the fibrinogen solution, at a concentration of 5×10^6 cell/mL. The cell and spheroid solution were mixed with thrombin (0.5 U/mL, Sigma, Burlington, MA, USA) and then immediately introduced into a central channel and settled at the bottom of the channel. Because the diameter of the spheroid ($>500 \mu\text{m}$) was greater than the channel height (150 μm), the spheroid was set to be stationary at the bottom of the channel. When the spheroid-ECs gel suspension was injected, an excess amount of the HUVEC and gel flowed out through the other two outlets of the center channel and did not leak to the media channel. The spheroid-ECs suspended gel was allowed to clot for 5 min at room temperature. Next, LFs at a concentration of 5×10^6 cell/mL were suspended in the fibrinogen solution, mixed with thrombin (0.5 U/mL, Sigma) and then immediately injected into the left and right stromal cell culture channel. The inlet reservoirs of the cell culture medium channels were loaded with EGM-2 media, and then the culture medium was aspirated at the other reservoir to fill media channels. Following loading all four reservoirs, the microfluidic platforms were incubated at 37 °C and 5% CO_2 . For EC-LEC tumor vascularized spheroid formation, tumor spheroid was collected from a 96-well plate using a 200 μL pipette tip and mixed with ECs and LECs suspensions in the fibrinogen solution, at a concentration of 5×10^6 cell/mL, respectively. The cells and spheroid solution were mixed with thrombin (0.5 U/mL, Sigma) and then immediately introduced into a central channel and settled at the bottom of the channel. The subsequent process is the same as the above-mentioned process.

2.4. Immunostaining

Samples were fixed with 4% (v/v) paraformaldehyde in PBS for 5 min, followed by 15 min permeabilization using a 0.15 % Triton X-100 (Sigma) and 1 h treatment of 3% bovine serum albumin (Sigma). The following primary antibodies were probed; fluorescein isothiocyanate (FITC)-conjugated anti-Albumin (GTX02090, GeneTex, Irvine, CA, USA), Alexa Fluor® 594-conjugated anti-human CD31 (eBioscience, San Diego, CA, USA), Alexa Fluor® 647-conjugated anti-human CD31 (303112, BioLegend, San Diego, CA, USA), Alexa Fluor® 488-conjugated Phalloidin (A12379, Invitrogen, Waltham, MA, USA), Alexa Fluor®488-conjugated anti-Ki67 (350508, BioLegend), Alexa Fluor® 488-conjugated VE-cadherin (53144942, Invitrogen, Waltham, MA, USA) and Hoechst 33342 (H1399, Invitrogen). The samples were washed three times and stored in PBS before imaging.

2.5. Terminal deoxynucleotidyl transferase dUTP nick end labeling (TUNEL)

TUNEL assay (ab66108, Abcam, Cambridge, UK) was performed according to the manufacturer's protocol. Briefly, each spheroid was fixed in 4% paraformaldehyde and embedded in an embedding medium (Tissue-Tek® O.C.T. Compound, Sakura Finetek, USA), then sliced into 14 μm -thick with a cryostat. The sectioned samples were washed with $1 \times$ PBS for 30 min and incubated in a permeabilization solution (0.1% Triton X-100 and 0.1% sodium citrate) for 2 min at room temperature. TUNEL mixture solution was added to the sectioned samples and incubated in a humidified chamber for 60 min at 37°C in a dark place. The sectioned samples were washed three times with $1 \times$ PBS and stained with Propidium iodide (PI).

2.6. Imaging and image processing

Tumor spheroid images were obtained from bright-field image or confocal microscope (Olympus FV1000, Japan and Zeiss LSM 880, Germany). The boundary of the tumor spheroid was detected and measured using ImageJ software. The 3D reconstruction and cross-section of the vessels were imaged using a confocal microscope. The microscope and charge-coupled device camera were controlled by MetaMorph (Molecular Device, San Jose, CA, USA) software for time-lapse imaging. 3D rendering and visualization of volume images of spheroid and tumor angiogenesis were performed using the Imaris software (Bitplane, UK). Blood vessels (volume and number of disconnected blood vessels) and spheroids were reconstructed using surface tools in Imaris software. In detail, to obtain the number of disconnected blood vessels, we did not split touching objects and the number of voxels were obtained from Imaris software. The resulting reconstructed blood vessels and spheroids were used for further analyses. GFP-labeled nanoparticles (mesoporous silica nanoparticles; MSN) were prepared according to the previously reported methods [36] and fluorescent spots of nanoparticles were reconstructed using the spot tool in Imaris software.

2.7. Anti-angiogenic compound treatment

Axitinib (Selleckchem) were reconstituted in DMSO according to the manufacturer's instruction. Axitinib was treated at the concentration of 1 nM and 10 nM, respectively for 4 days. We administered axitinib-containing medium prevascularization and postvascularization and refreshed it every 24 h for 3 days. In prevascularization, axitinib was administered prior to the formation of the 3D vascular network adjacent to the tumor spheroid. In postvascularization on day 4 following vascularization on the VTS chip, axitinib-containing media was replaced into the microfluidic reservoir.

2.8. RNA sequencing

Total RNA was extracted from spheroids by using TRIzol reagent (Invitrogen). Following the manufacturer's instructions, the library was constructed by using a QuantSeq 3' mRNA-Seq Library Prep Kit (Lexogen, Austria). Subsequently, single-end 75 high-throughput sequencing was performed using NextSeq 500 (Illumina, USA) and RNA-seq reads were aligned to the reference genome (UCSC hg19). Then, genes of more than 2 fold changes and less than p -value 0.05 between HepG2 only spheroids and 1:1 hybrid spheroids were regarded as differentially expressed genes (DEGs). Both clustering heatmaps and volcano plot of DEGs were generated using ExDEGA GraphicPlus v.3.0.3 (eBiogen, Republic of Korea). DEGs were also

subjected to gene ontology (GO) analysis using DAVID Bioinformatics resources (<https://david.ncicrf.gov/tools.jsp>). For overrepresented GO biological processes (GO: 0030334 and 0016477), top 20 upregulated genes in the 1:1 hybrid spheroids were presented as a heatmap of z-score values using ExDEGA GraphicPlus program. For gene set enrichment analysis (GSEA), 1:1 hybrid spheroid was compared to HepG2 only spheroid using the GSEA v4.2.3 program. The number of permutations was set to 1000, and the permutation type was “gene set”. “Diff_of Classes” was used as a metric for ranking genes. The National Center for Biotechnology Information Gene Expression Omnibus (GEO) accession number for the RNA-seq data reported in this study is GSE212669.

2.9. Western blot

Protein lysates from each spheroid or HepG2 cells indirectly co-cultured with HUVECs by using a transwell system were obtained by using Pro-prep (iNtRON Biotechnology, Republic of Korea). The samples were separated by 8–12% of SDS-PAGE gels and transferred to the 0.2 μm nitrocellulose membranes. After blocking with 3% bovine serum albumin (GenDEPOT, Katy, TX, USA) for an hour at room temperature, the membranes were probed with the following primary antibodies at 4 °C overnight: β -actin (3700, Cell Signaling Technology, Danvers, MA, USA), α -SMA (ab184675, Abcam), MMP-9 (AB19016, Sigma), SLUG (ab27568, Abcam), p53 (2524, Cell Signaling Technology), Vimentin (5741, Cell signaling technology) and E-cadherin (14472, Cell signaling technology). Subsequently, the membranes were incubated with HRP-conjugated secondary antibodies (Invitrogen) for an hour at room temperature. To detect the protein bands, Clarity Western ECL substrate (BR1705061, Bio-Rad, Hercules, CA, USA) was used and the bands were visualized by using ChemiDoc MP Imaging System (Bio-Rad). Each protein band was quantified by using Image J and the expression of target protein was normalized with the expression of β -actin.

2.10. Quantitative RT-PCR (qRT-PCR)

Total RNA was extracted from HUVECs co-cultured with HepG2 in a transwell system using TRIzol reagent according to the manufacturer's instructions. Complementary DNA was then synthesized from the extracted RNA using Superscript III First-Strand Synthesis System (Invitrogen). Quantitative Real-time RT-PCR was performed with SYBR Green PCR Master Mix (Applied Biosystems, Waltham, MA, USA) using ABI 7300 Real time PCR system (Applied Biosystems). 5 μM of forward primer and reverse primer were used for amplification. Relative quantification of target mRNA expression levels was determined by $2^{(\Delta\Delta \text{threshold cycle})}$ method. The expression level of each gene was normalized to GAPDH. At least three independent experiments were performed. The sequences of primers used are included in Supplementary Table 1.

2.11. Permeability coefficient measurement

To calculate the permeability coefficient, fluorescence images of 70 kDa FITC-dextran (Sigma) solutions were introduced into one of the two remaining media reservoirs. An open, perfusable microvessel allowed solution perfusion into the lumen. 10 x magnification pictures were obtained at 10 s intervals over 10 min using time-lapse mode in a confocal microscope.

The derivation process for this equation was detailed in a previous paper from our group [37]. The permeability coefficient P was derived using the equation below:

$$P = 1/l_w \times (dl/dt)/I_j$$

l_w is the length of the vessel wall from the micropost that separates the microvessel from the perivascular region. I_j is the mean

intensity in the microvessel region and I is the total intensity in the perivascular region.

2.12. CUBIC tissue clearing

To prevent loss of 3D blood vessels and spheroid information, we used CUBIC tissue-clearing protocols based on hydrophilic reagents that preserve fluorescence [38]. ScaleCUBIC-1 was prepared as a mixture of 10 wt% urea (Nacalai Tesque Inc., 35904-45, Japan), 5 wt% N,N,N',N'-tetrakis (2-hydroxypropyl) ethylenediamine (Tokyo Chemical Industry CO., LTD., T0781, Japan), and 10 wt% Triton X-100 (VWR Life Science, AAA16046-AE, USA). ScaleCUBIC-2 was prepared as a mixture of 50 wt% sucrose (Nacalai Tesque Inc., 30403-55, Japan), 25 wt% urea, 10 wt% triethanolamine (Sigma-Aldrich, T58300, USA). After sample fixation, we introduced the ScaleCUBIC-1 solution into the medium channel for 1 week and conducted immunohistochemistry analysis. ScaleCUBIC-2 solution for RI (refractive index) matching was introduced 1 day before confocal imaging.

2.13. Statistical methods

Prism (GraphPad, USA) was used for one-way ANOVA analysis with Tukey's post-test. *** denotes $p < 0.001$, ** denotes $0.001 < p < 0.01$, * denotes $0.01 < p < 0.05$. For significant testing between two conditions non-paired student's t-test was used. All data were expressed as the mean \pm standard deviation (SD).

3. Results

3.1. Establishment of self-assembled 3D vascularized tumor spheroid model

Tumor development occurs in two stages. When the tumor is relatively small, no neovessels have yet developed to provide nutrients and oxygen to tumor cells; however, as the tumor grows, tumor cells stimulate ECs to initiate angiogenesis for tumor vascularization [39]. The interactions between the tumor and blood vessels ultimately lead to the systemic spread of malignant tumor cells throughout the whole body (i.e., metastasis). To engineer a vascularized tumor model at the chip level, a tumor spheroid in which HepG2 cells and HUVECs (1:1 ratio, total 5000 cells) were aggregated, and the HUVEC suspension was mixed with fibrin gel and loaded into the center channel of a microfluidic chip. LF-laden fibrin gel was also introduced to provide the matrix proteins needed for angiogenesis (Fig. 1a). We first validated that the HepG2-EC hybrid spheroid successfully grew in size within the fibrin matrix. Assessment of the spheroid growth in the device was performed 6 days ($122.3 \pm 2.3\%$) after implantation and demonstrated significant growth of the spheroid compared to that on day 1 ($100.0 \pm 1.5\%$) (Fig. 1b,c). Following HUVEC elongation at day 1, the formation of a dense vascular network and lumen structures was observed after 6 days of culturing (Fig. 1b-d). The relative blood vessel area on day 6 was 1.8-fold greater than that on day 1 (Fig. 1e).

3.2. Development of tumor-EC hybrid spheroids

It had been previously reported that as cancer progressed to a high degree of malignancy, blood vessels formed not only around the tumor but also inside the tumor [40]. Hence, we generated tumor-EC hybrid spheroids to mimic the intratumoral vasculature and investigated the significance of coculturing tumor cells and ECs within these spheroids. Tumor-EC hybrid spheroids were established from a total of 5000 cells by mixing HepG2

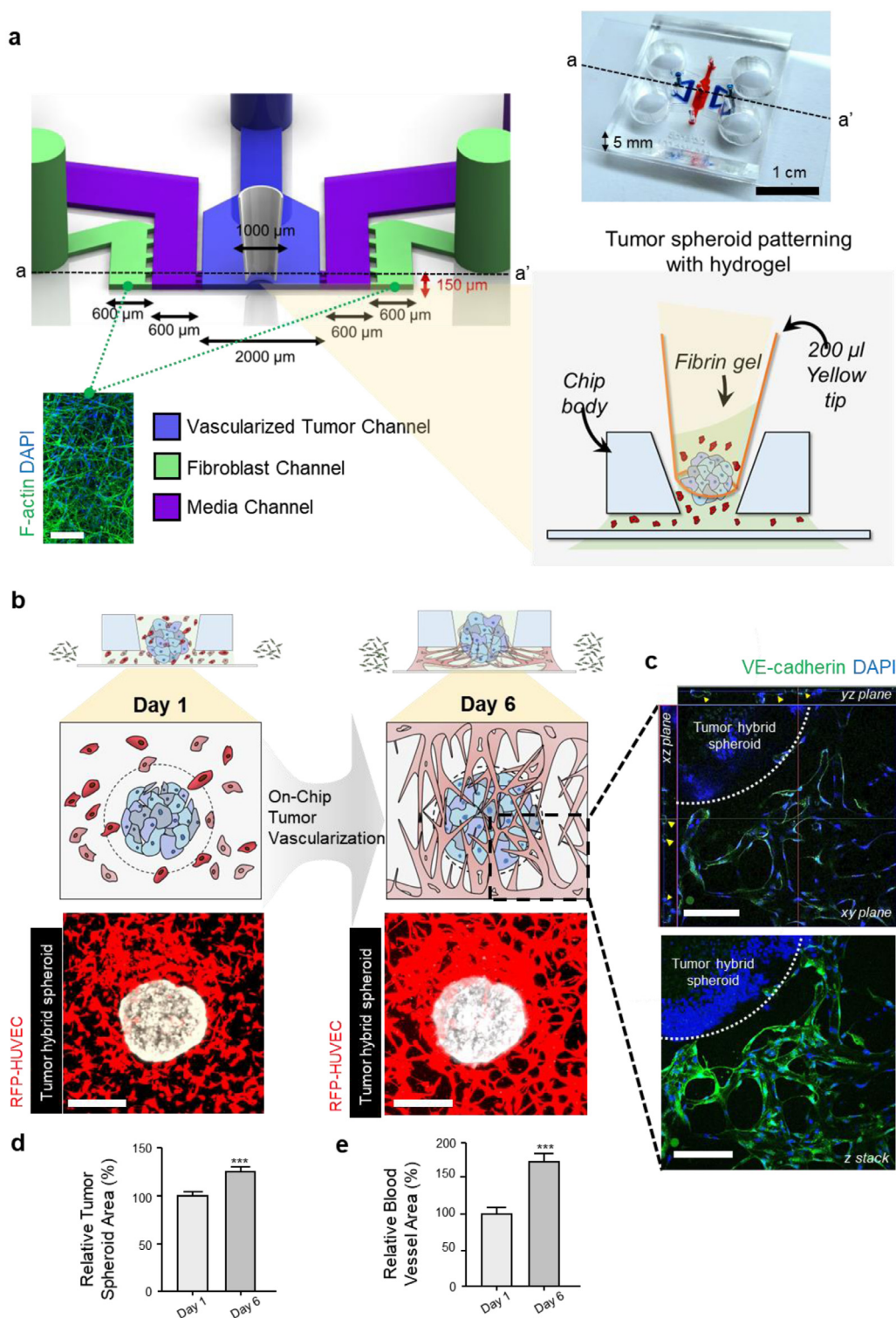


Fig. 1. *In vitro* three-dimensional vascularized tumor model. (a) Schematic representation of microfluidic device designed for *in vivo*-like 3D vascularized tumor formation by tumor spheroid and ECs mixture in the center channel under paracrine interactions with stromal fibroblasts in the outermost side channels. Representative confocal image shows fibroblasts in 3D fibrin gel. (Scale bar, 150 μm) (b) Schematic representation and confocal images of the development of vascularized tumor spheroid, composed of tumor spheroid enveloped by endothelial cells. (Scale bars, 400 μm) (c) Vascular network (VE-cadherin, green) and xyz plane confocal image demonstrated lumen structures of vascular network (yellow arrows). (Scale bars, 150 μm) (d) Relative spheroid growth area of day 0 and day 6. ($n = 6$) (e) Relative blood vessel area of day 0 and day 6. ($n = 6$) All data were expressed as the mean \pm SD, *** $p < 0.001$ versus Day 1. (For interpretation of the references to colour in this figure legend, the reader is referred to the web version of this article.)

cells and HUVECs in different ratios (4:1 and 1:1). These hybrid spheroids were compared with spheroids composed of only HepG2 cells by analyzing their morphological appearance, proliferation rate and cancer cell progressiveness. First, we examined the sphericity of each spheroid, which was calculated by the ratio of the major axis to the minor axis. While both HepG2-only spheroids and 4:1 hybrid spheroids had flat and atypical shapes, the 1:1 hybrid spheroids exhibited the greatest sphericity (Fig. 2a,b). Furthermore, tissue clearing by CUBIC allowed us to visualize the markers expressed inside the tumor spheroid. With this strategy, we verified that both HepG2-only spheroid and hybrid spheroids were proliferating, as indicated by the Ki-67 expression (Fig. 2c,d). In addition, TUNEL assay results showed that cell apoptosis was not significantly detected in the spheroids from all groups. (Fig. 2e,f). In addition, there was no statistical difference in the viability of all groups (Supplementary Fig. S2). As expected, Albumin (hepatocyte-specific marker) was expressed throughout the spheroids, whereas the expression of CD31 within the hybrid spheroid was significantly increased as the EC ratio was increased (Fig. 2g,h).

3.3. Increased aggressiveness of tumor-EC hybrid spheroids

Next, to gain insight on how ECs embedded in the spheroid can affect cancer cells, we performed RNA sequencing of HepG2-only spheroid and tumor-EC hybrid spheroids on day 4. After a total of 709 DEGs in the 1:1 hybrid spheroids compared to the HepG2 only spheroids were sorted, the expression patterns of these genes were visualized as a clustering heatmap (Fig. 3a). Notably, the 1:1 hybrid spheroids showed distinct gene expression patterns compared to the 4:1 hybrid spheroids and the HepG2-only spheroids, suggesting the significant transcriptional changes in the 1:1 hybrid spheroids. GO analysis revealed that DEGs in the 1:1 hybrid spheroids were primarily enriched in the biological processes including cell migration, vasculature development, cell motility and proliferation (Fig. 3b). Accordingly, the clustering heatmap showed a drastic upregulation of genes associated with cell migration in the 1:1 hybrid spheroids relative to the other groups (Fig. 3c). Furthermore, GSEA results indicated an enrichment for p53 signaling pathway KEGG gene set in the HepG2-only spheroids compared to 1:1 hybrid spheroids, implying the enhanced aggressiveness of 1:1 hybrid spheroids via suppression of p53 pathway (Fig. 3d). In the volcano plot created with transcriptomic profiles of HepG2-only spheroids and 1:1 hybrid spheroids, we identified that not only vascular gene set (*PECAM1*, *VWF*, and *FLT1*) but also the genes associated with cancer progression, invasion and metastasis including *VIM* [41], *H19* [42], *LAMB3* [43], *ITGA5* [44], and *IGFBP5* [45], were significantly upregulated. Furthermore, we examined the expression of proteins that are associated with cancer cell migration in each spheroid group. The epithelial-mesenchymal transition (EMT) is a process in which molecular alterations enable epithelial cells to gain mesenchymal properties and thus undergo migration and invasion, which are required for the invasive and metastatic outgrowth of hepatocellular carcinoma [46]. Notably, we found that the expression of Vimentin, an EMT regulator, was upregulated in the 1:1 hybrid spheroids compared to that in the HepG2-only spheroids, which was consistent with RNA sequencing results (Fig. 3e–g). We also observed a significant increase in mesenchymal marker (SLUG, MMP-9 and α -SMA) expression because of EMT induction in the 1:1 hybrid spheroids (Fig. 3f,g). Accordingly, loss of E-cadherin (epithelial marker) expression, a hallmark of EMT induction, was evident in the 1:1 hybrid spheroid (Fig. 3f,h). Moreover, the expression of the p53 was markedly decreased in the 1:1 hybrid spheroid relative to that in the HepG2-only spheroid, implying that the 1:1 hybrid spheroid was more aggressive than the

HepG2-only spheroid (Fig. 3f,i). Since HepG2 cells and ECs were randomly mixed in the hybrid spheroid, HepG2 cells were also indirectly cocultured with ECs in a transwell system to determine the cellular origin of the expression patterns. Consistently, HepG2 cells cocultured with ECs showed higher expression of EMT-related proteins than HepG2 cells cultured without ECs (Supplementary Fig. S3a,b). Moreover, p53 expression in the HepG2 cells cocultured with ECs was significantly decreased compared to that in the HepG2 cell-only culture (Supplementary Fig. S3a,c). These results indicated that HepG2 cells showed increased aggressiveness when cocultured with ECs because of the inhibition of tumor suppressors and induction of the EMT. Taken together, we established the solid tumor spheroids maintaining spherical morphology and aggressive properties by combining tumor cells and ECs in a 1:1 ratio.

3.4. Reconstituting vascularized tumor spheroid on a chip

Because tumor cells can interact with neighboring blood vessels in multiple ways, we next evaluated the effects of the tumor-EC hybrid spheroid on the acceleration of peritumoral angiogenesis (Fig. 4a). We fabricated a vascularized tumor spheroid (VTS) chip by introducing a HUVEC suspension containing HepG2-only spheroids or 1:1 tumor-EC hybrid spheroids. The tumor-EC hybrid spheroids significantly increased the total volume of blood vessels around the spheroids compared to the HepG2-only spheroids (Fig. 4a,b) while there was no statistical difference in tumor spheroid area without or with HUVEC coculture (Supplementary Fig. S4). To elucidate the molecular changes of the ECs induced in coculture with tumor cells, we indirectly cocultured HUVECs with HepG2 cells in a transwell system and subsequently performed qRT-PCR. The mRNA expression of angiogenic genes, including *VEGFR2*, *VE-cadherin*, *VEGF* and *vWF*, was significantly upregulated in HUVECs cocultured with HepG2 cells compared to the HUVECs cultured without HepG2 cells (Fig. 4c). These combined results indicated that the crosstalk between tumor cells and ECs promoted tumor angiogenesis. In addition, to verify that peritumoral vessels were interconnected within intratumoral vessels, we injected fluorescently labeled silica nanoparticles into the peritumoral vasculature using a syringe pump at a rate of 450 μ L/h (Fig. 4d). The results showed that the silica nanoparticles were gradually distributed throughout the vasculature (Fig. 4d,e). Eventually, after 60 min, some nanoparticles reached the center of the spheroid, suggesting that the tumor-associated vasculature may serve as an irrigation system resembling the physiological state (Fig. 4f–h). In summary, our VTS model successfully recapitulated aggressive solid tumors in which intratumoral vessels were interconnected to peritumoral vessels at the chip level.

3.5. Evaluation of permeability of tumor-associated vasculature

Tumor vasculature has been regarded as aberrantly leaky due to an abnormal vascular basement membrane and lower pericyte coverage [47, 48]. Therefore, we attempted to validate that our VTS model reflected the unique features of tumor-associated vasculatures, including permeability and FIOs (Fig. 5a,b). We introduced solutions containing FITC-dextran tracers (70 kDa) into the peritumoral vasculature on the VTS chip and visualized FITC-dextran leakage and FIOs in 10 s intervals (Fig. 5c). Then, the apparent permeability coefficient was calculated as described in the Materials & Methods section. We first observed endothelial pores corresponding to FIOs in the vasculature, especially adjacent to the tumor spheroid (Fig. 5c). The number of FIOs was significantly increased in vascularized tumors compared to that

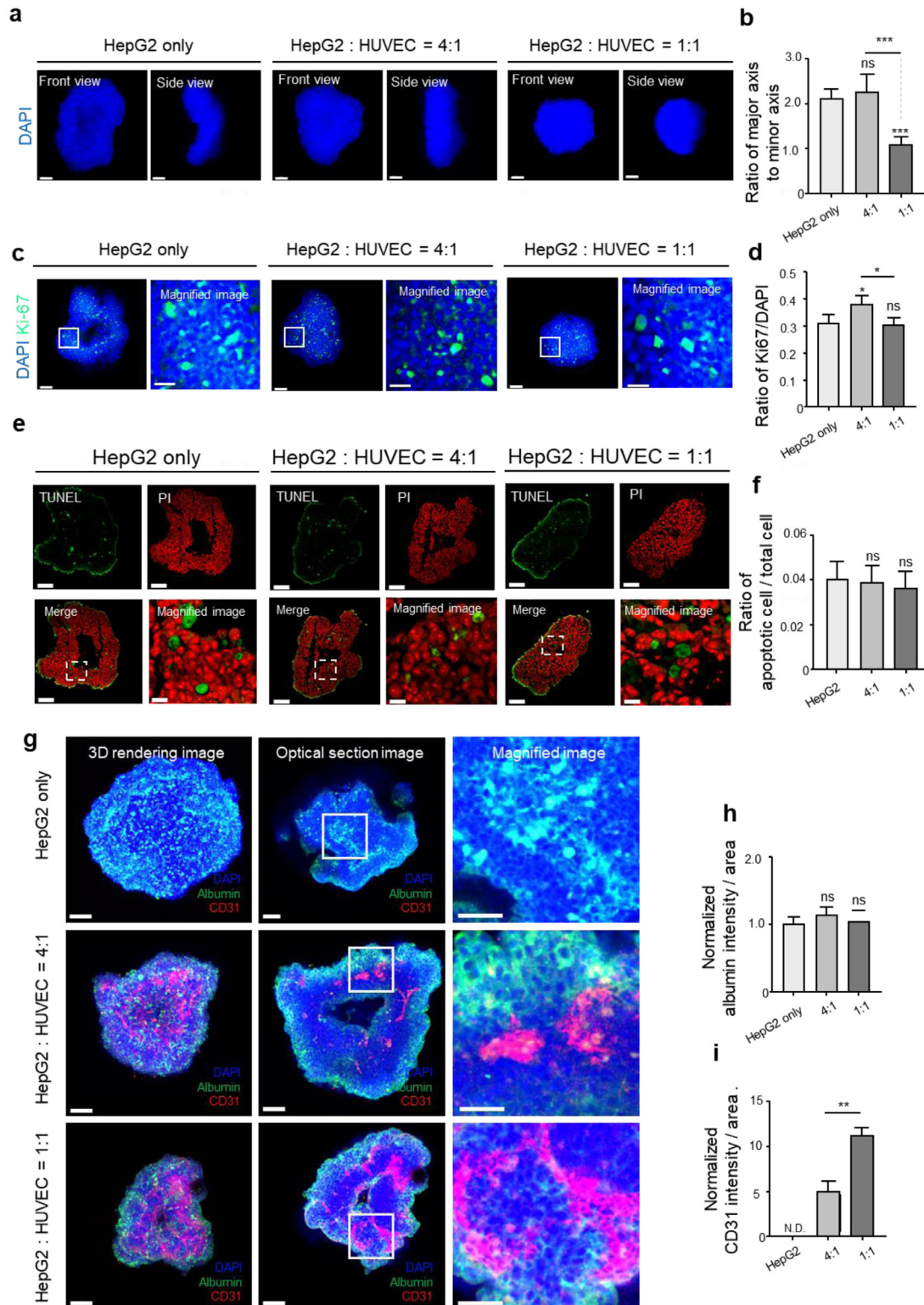


Fig. 2. Characterization of multicellular tumor spheroids. (a) Representative confocal images (a) of tumor spheroids with different EC ratio fixed at day 5. (Scale bars, 200 μm) (b) Quantification of the sphericity of the spheroids in each group. ($n = 6$) (c-d) Confocal images of spheroids stained with Ki67 (green) (c) and quantification Ki-67⁺ cells (d) within each spheroid. DAPI was used for nuclei staining. ($n = 6$) (e) TUNEL assay (TdT enzyme, green) was performed with each spheroid to analyze the apoptosis. Nuclei was stained with PI (red). (Scale bars, 100 μm and Magnified image: Scale bars, 20 μm) (f) Quantification of apoptotic rate within the spheroids. ($n = 6$) (g) Confocal images of spheroids stained with DAPI (nuclei, blue), Albumin (green) and CD31 (red). (3D rendering image and optical section image: Scale bars, 100 μm and Magnified image: Scale bars, 50 μm) (h-i) Quantification of the fluorescence intensity of Albumin (h) and CD31 (i) within the spheroids. ($n = 6$) All data were expressed as the mean \pm SD. One-way ANOVA analysis with Tukey's post-test. * $p < 0.05$, ** $p < 0.01$, *** $p < 0.001$, n.s. not statistically significant, versus HepG2 only. N.D.; not detected. (For interpretation of the references to colour in this figure legend, the reader is referred to the web version of this article.)

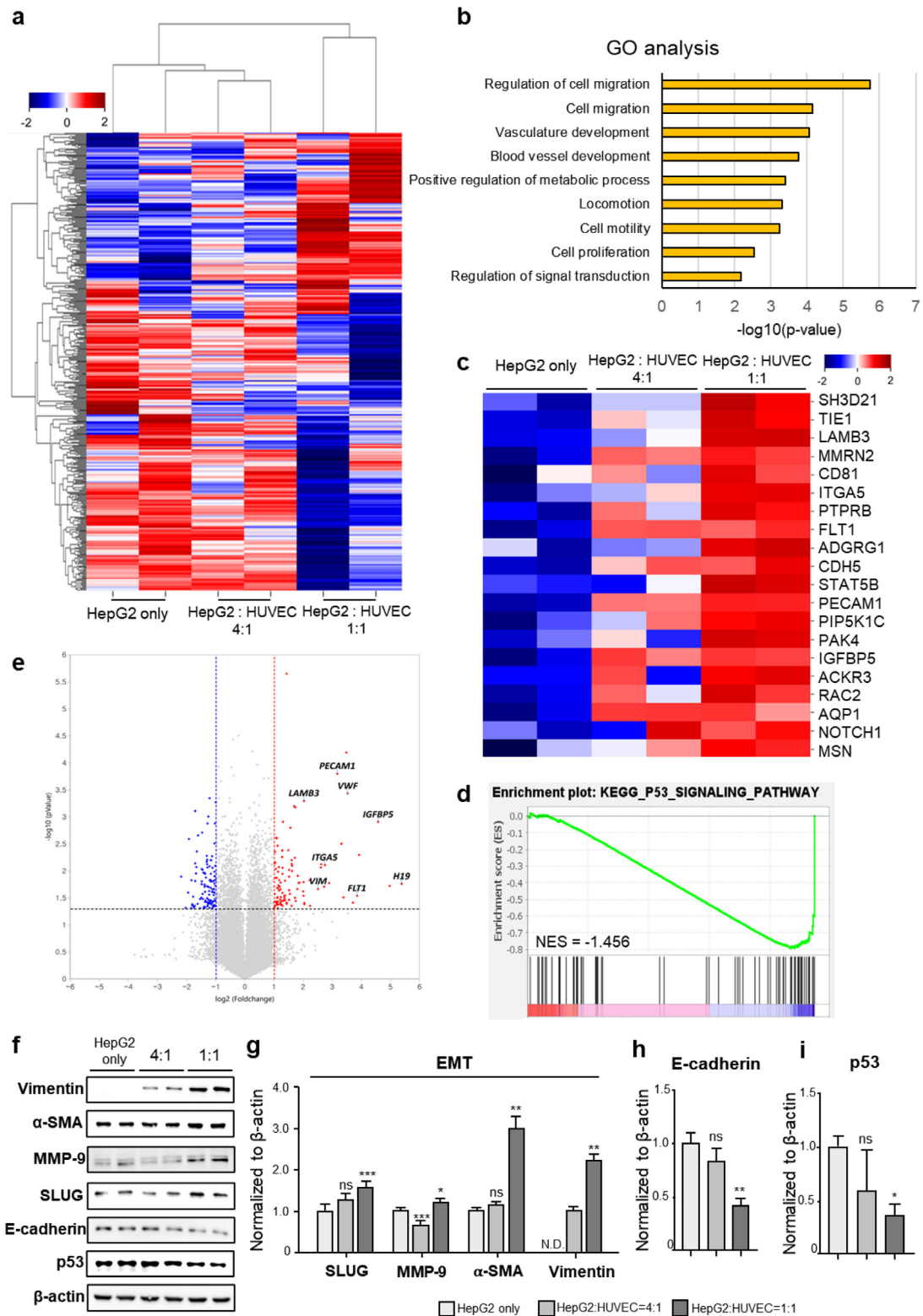


Fig. 3. RNA sequencing and protein expression of tumor spheroids. (a) Clustering heatmap showing the expression pattern of DEGs in HepG2-only spheroids, 4:1 hybrid spheroids and 1:1 hybrid spheroids, analyzed from mRNA QuantSeq. ($n = 2$) (b) GO terms over-represented in a set of DEGs (fold change ≥ 2.0 , p -value ≤ 0.05) in the 1:1 hybrid spheroids compared to the HepG2 only spheroids. (c) Heatmap showing the expression pattern of top 20 upregulated genes in cell migration gene set in HepG2 only spheroids and tumor-EC hybrid spheroids. (d) GSEA of DEGs in HepG2 only spheroids and 1:1 hybrid spheroids, indicating the enrichment of p53 signaling pathway. (e) Volcano plot showing all DEGs in HepG2 only spheroids and 1:1 hybrid spheroids, analyzed from mRNA QuantSeq. (f-i) Western blot analysis (f) and quantification of EMT markers (SLUG, MMP-9, α -SMA, and Vimentin; g), E-cadherin (epithelial marker; h) and p53 tumor suppressor (i) in HepG2 only spheroids and hybrid spheroids. ($n = 3$) All data were expressed as the mean \pm SD. One-way ANOVA analysis with Tukey's post-test. * $p < 0.05$, ** $p < 0.01$, *** $p < 0.001$, n.s. not statistically significant, versus HepG2 only. N.D.; not detected.

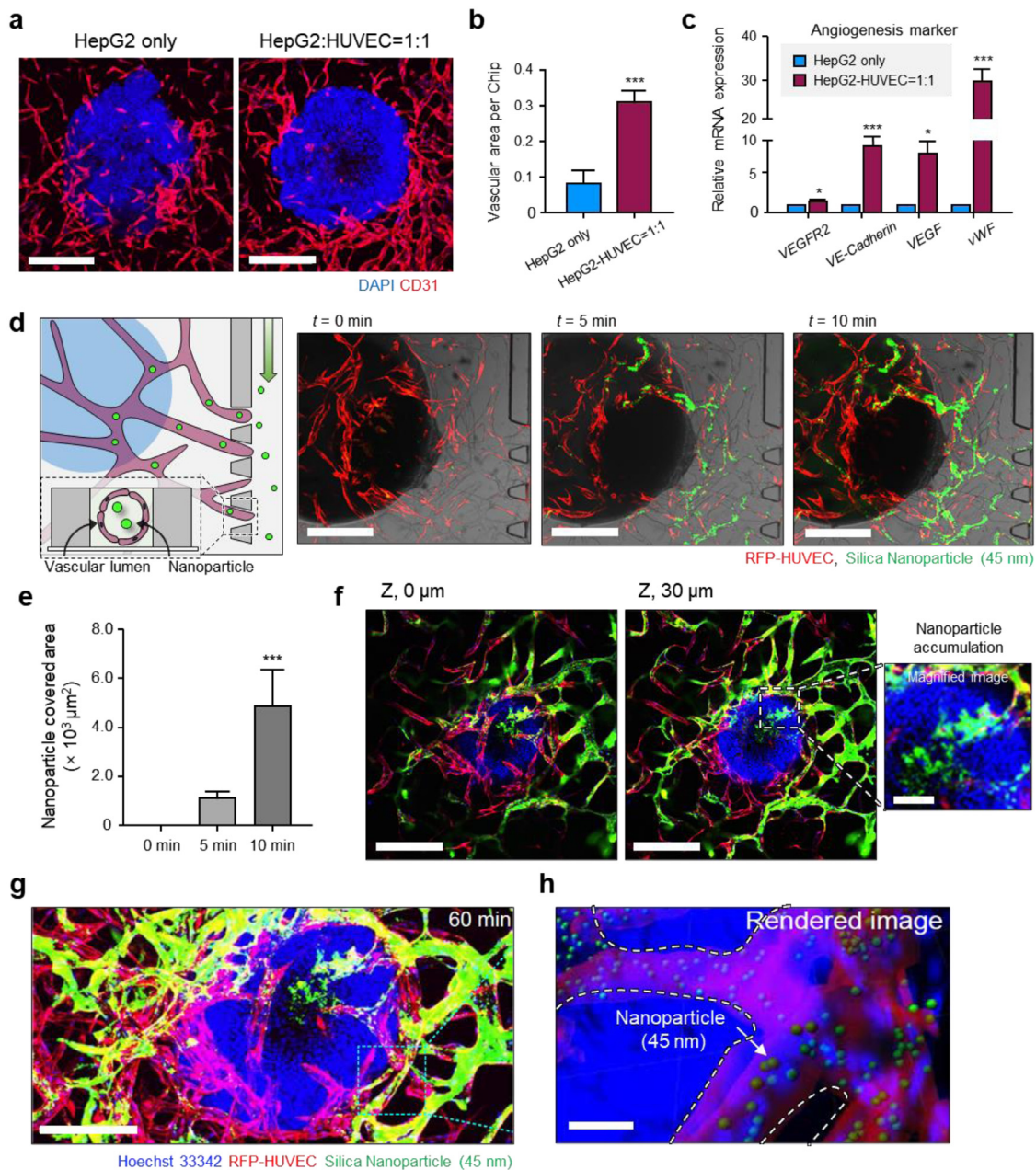


Fig. 4. Recapitulation of peritumoral vasculature interconnected with tumor spheroid in VTS chip. (a–b) Representative confocal images (a) and quantification (b) of peritumoral angiogenesis in VTS model using HepG2 only spheroid and tumor-EC hybrid spheroid. (Scale bars, 400 μm , $n = 6$). (c) qRT-PCR analysis of genes related to angiogenesis in 2D-cultured HepG2 cells and HepG2 cells indirectly cultured with HUVECs. The internal standard housekeeping gene was GAPDH. ($n = 3$) (d) Schematic diagram and time-dependent confocal images of silica nanoparticle delivery into the tumor spheroid via peritumoral vasculature. (Scale bars, 400 μm) (e) Quantification of the area in which nanoparticles are covered at 0, 5 and 10 min after injection. ($n = 3$) (f) Silica nanoparticle distribution at different z sections. (Scale bars, 400 μm and magnified image: Scale bar, 100 μm) (g) Representative confocal images of distributed nanoparticles at 60 min after injection. (Scale bar, 200 μm) (h) Rendered image of nanoparticle flow from peritumoral vasculature to intratumoral vasculature. (Scale bar, 50 μm) All data were expressed as the mean \pm SD. One-way ANOVA analysis with Tukey's post-test. * $p < 0.05$, *** $p < 0.001$ versus control.

in the HUVEC-only control (Fig. 5d). In addition, the mean apparent permeability value of the vasculature (with no tumor spheroids) was $0.24 \times 10^{-5} \pm 3.17 \times 10^{-7}$ cm/s, which was significantly lower than that of the tumor-EC hybrid spheroid ($1.32 \times 10^{-5} \pm 2.5 \times 10^{-6}$ cm/s) (Fig. 5e). Therefore, ECs located near tumor tissue may have formed loose interconnections, demonstrating the abnormality of tumor-associated vessels. To elucidate the molecular changes in inflammation and regulation of vascular permeability by ECs induced in coculture with tumor cells, we performed qRT-PCR. The mRNA expression of *ICAM1* was significantly upregulated in HUVECs cocultured with HepG2 cells compared to HUVECs cultured alone (Fig. 5f).

3.6. Anti angiogenic drug response in pre/post tumor spheroid vascularization

Axitinib, a Federal Drug Administration (FDA)-approved anti-cancer drug, is a potent and selective tyrosine kinase inhibitor that targets receptors involved in angiogenesis: VEGFR 1, 2, and 3 and platelet-derived growth factor receptor (PDGFR) [49]. Therefore, we attempted to verify both the antitumor and antiangiogenic activities of axitinib in our VTS model. Before we treat axitinib in our VTS model, we first decided to investigate the correlation between viability and the size of tumor-EC hybrid spheroids treated with different dosages of axitinib (0 nM, 1 nM, and 10 nM)

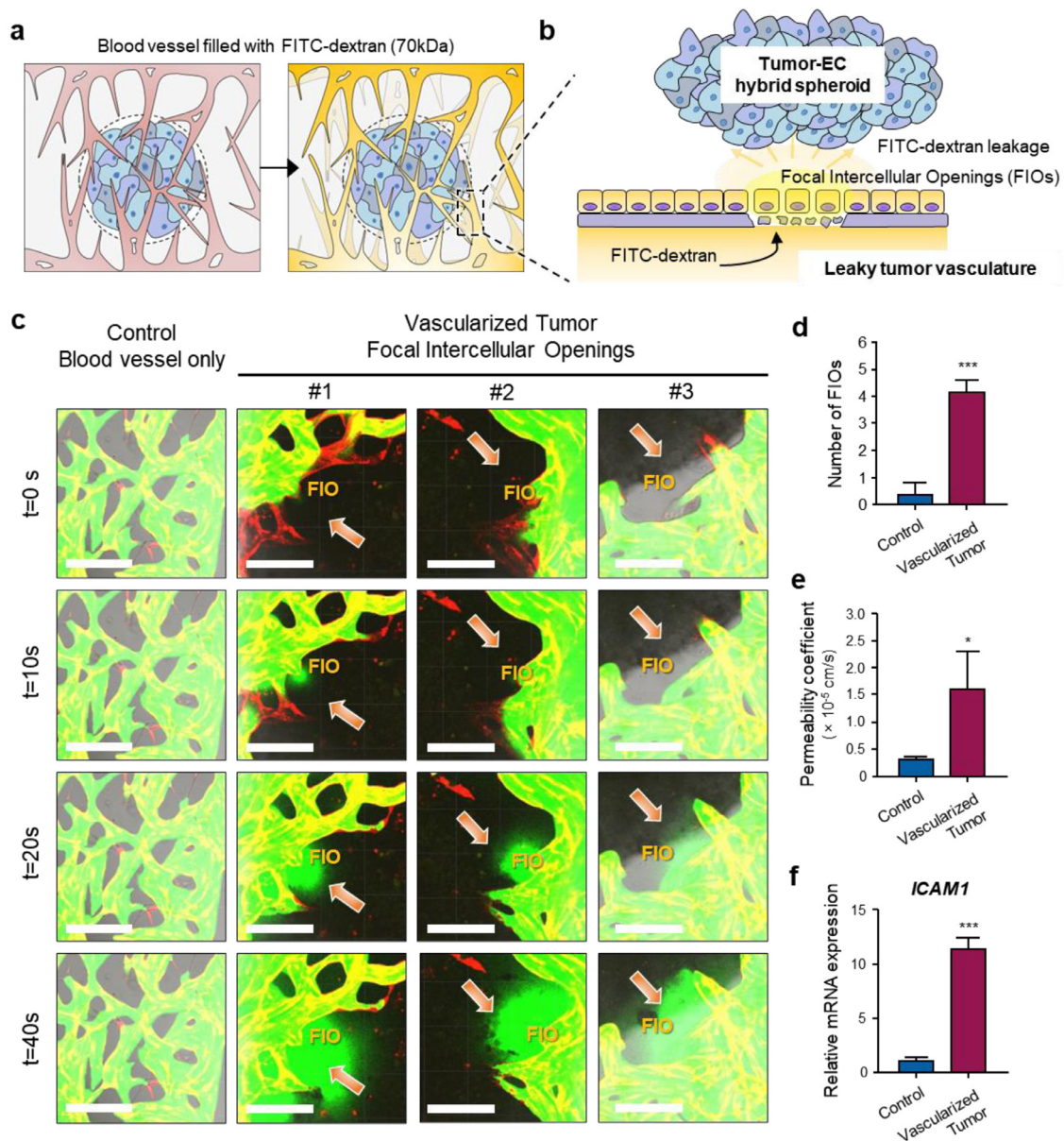


Fig. 5. Assessment of tumor vessel permeability. (a-b) Schematic illustration of permeability evaluation by measuring dextran leakage via FIOs formed in tumor vasculature. (c) Time series fluorescence micrographs were taken and analyzed for intensity changes in the perivascular region to measure permeability. After the FITC-dextran (70 kDa) solution was introduced, images were captured every 10s. Control represents blood vessel culture without tumor spheroid. FIOs (arrows) are observed in tumor spheroid co-culture conditions. (Scale bars, 150 μ m) (d) Quantification of the number of FIOs. ($n = 6$) (e) Calculated permeability coefficient of control vessels and vessels in VTS chips. ($n = 6$) (f) qRT-PCR result of *ICAM1* expression in control vessels and vessels in VTS chips ($n = 3$). All data were expressed as the mean \pm SD. * $p < 0.05$, *** $p < 0.001$, versus Control.

outside the chip. As a result, the viability of the tumor spheroids was reduced in a dose dependent manner (Supplementary Fig. S5a,b). Along with these results, the spheroid size was also decreased after axitinib treatment (Supplementary Fig. S5c). Thus, the positive correlation between the size and viability of the spheroids may allow us to infer the efficacy of axitinib targeting the tumor spheroids in the VTS chip. We next administered axitinib-containing medium prevascularization and postvascularization and refreshed it every 24 h for 3 days in the VTS chip. After prevascularization, 0 nM, 1 nM or 10 nM axitinib was administered prior to the formation of the 3D vascular network adjacent to the tumor spheroid (Fig. 6a). The area containing hybrid spheroids was not significantly changed, regardless of axitinib treatment (Figs. 6b,c and S3). However, axitinib significantly reduced the blood vessel volume and increased the number of dis-

connected blood vessels in a dose-dependent manner, indicating that the antiangiogenic effect of axitinib had been reproduced in our model (Fig. 6b,d,e). In contrast, when axitinib was administered postvascularization on day 4 following vascularization on the VTS chip (Fig. 6f), the 10 nM of axitinib-treated spheroids were remarkably smaller than the vehicle-treated spheroids, demonstrating the potentiation of the antitumor activities of axitinib (Fig. 6g,h). The blood vessels in the axitinib-treated groups regressed and were disconnected in a dose-dependent manner compared to those in the control group (Fig. 6g,i,j). These results underlined the significance of tumor vascularization required for drug delivery and reactions as well as for the interactions between the tumor and blood vessels. Thus, we proved that our VTS chip effectively reproduced the efficacy of anticancer drugs (Supplementary Fig. S6).

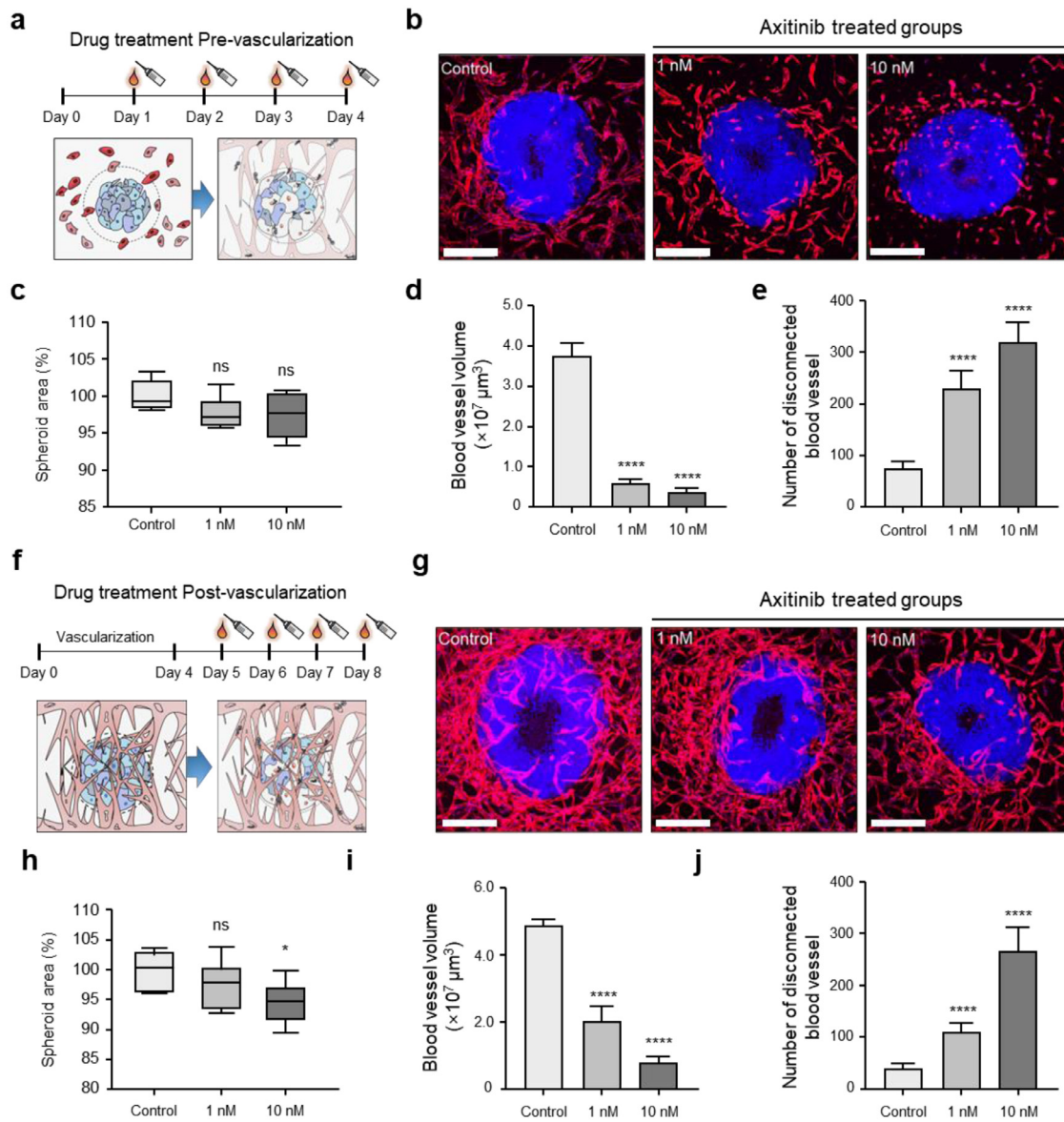


Fig. 6. Anti-angiogenesis and anti-tumor activities of Axitinib in the VTS model. (a) Axitinib treatment in the early stage of the VTS model. Axitinib were introduced into the reservoirs a day after tumor-EC gel suspension was injected to the central channel before tumor vascularization. (b) Representative confocal images showing dose-dependent response of spheroid and vasculature to Axitinib in the early VTS model. (Scale bars, $300 \mu\text{m}$) (c-e) Quantification of relative spheroid area (c), blood vessel area per device (d) and number of disconnected blood vessel per device (e) in response to two different doses of Axitinib (1 nM and 10 nM) at the early stage. (f) Axitinib treatment in the late stage of the VTS model. Axitinib was introduced into the reservoirs after vasculature fully enveloped tumor-EC hybrid spheroids on day 5. (g) Representative confocal images showing dose-dependent response of spheroid and vasculature to Axitinib in the late stage of VTS model. (Scale bars, $300 \mu\text{m}$) (h-j) Quantification of relative spheroid area (h), blood vessel area (i) and the number of disconnected blood vessels (j) in response to two different doses of Axitinib at the late stage of VTS model. All data were expressed as the mean \pm SD. One-way ANOVA analysis with Tukey's post-test. * $p < 0.05$, **** $p < 0.0001$, n.s. not statistically significant, versus Control.

3.7. Reconstituting lymphatic EC-blood vascular EC incorporated vascularized tumor spheroid in vitro

To create the TME, vasculotropic tumor cells that induce not only angiogenesis but also lymphangiogenesis and that remodeled preexisting lymphatics were used [50]. As lymphatic vessels are avenues of tumor intravasation and subsequent metastasis, blocking tumor-associated lymphangiogenesis is considered a promising therapy for alleviating malignancy [51]. Therefore, generating a new model in which blood vessels and lymphatic vessels are simultaneously patterned around the tumor spheroid was a worthwhile effort. Using our VTS chip, we introduced an EC-lymphatic EC (LEC) suspension (5×10^6 cells/mL each) with tumor-EC 1:1 hybrid spheroids in the center channel (Fig. 7a). To optimize the

culture conditions of the lymphatic system, we imposed a hydrostatic pressure gradient on the chip by adding different volumes of medium at either end of the media channel [52]. As a result, we observed that both the lymphatic and vascular networks exhibited direct physical contact with the tumor spheroids and formed an intricate irrigation system (Fig. 7b). Although the spheroid size was not correlated with the application of interstitial flow (Fig. 7b,c), the area occupied by blood vessels and lymph vessels was markedly increased with interstitial flow (Fig. 7b,d,e). In summary, we achieved advancements in VTS chips by presenting a complicated TME, including lymphatic and blood vessels, through interstitial flow stimulation. Considering the various roles of lymphatics in tumor progression, use of these approaches is essential for the development of drugs targeting tumor lymphangiogenesis.

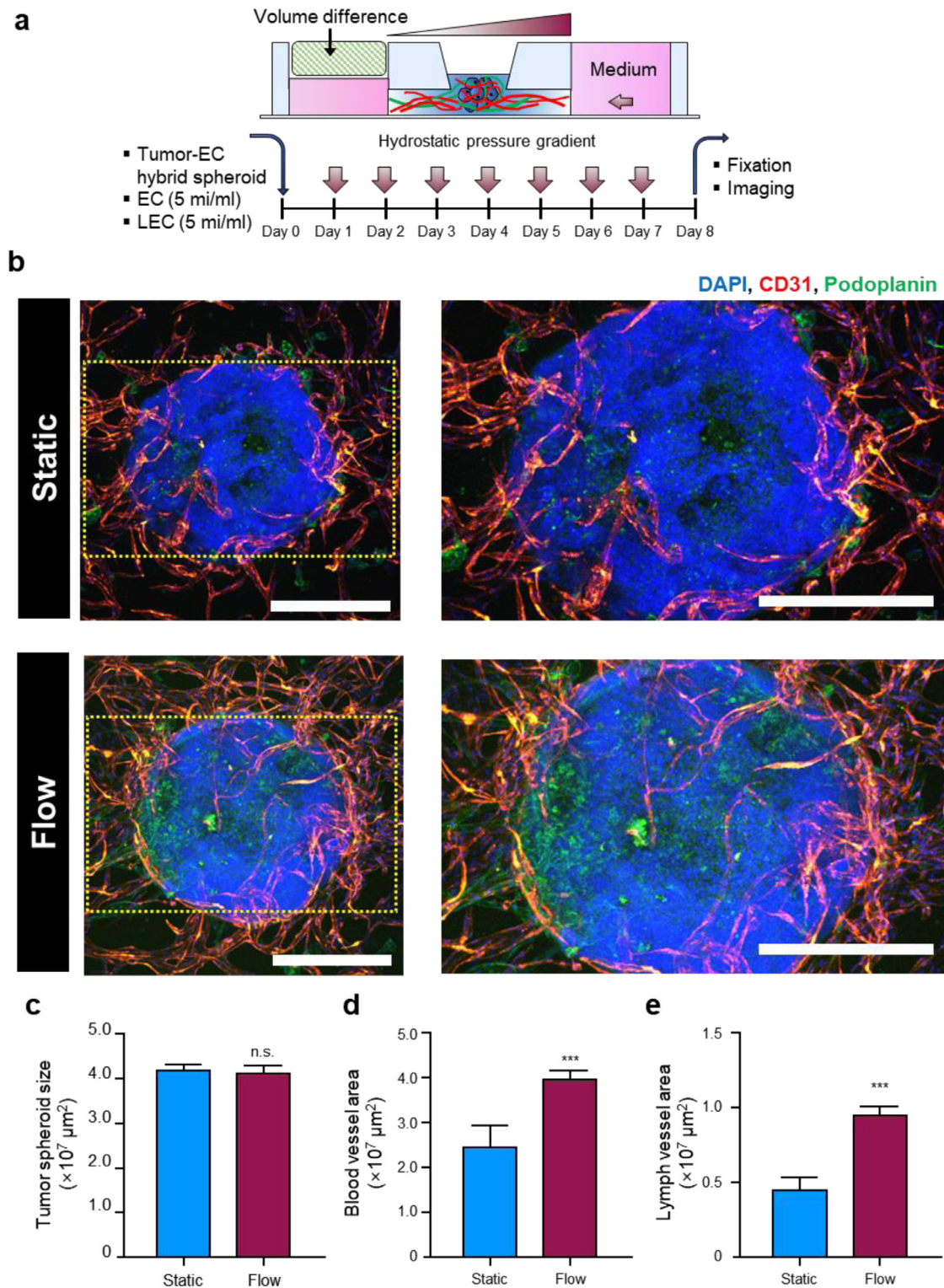


Fig. 7. Efficient lymphangiogenesis in the VTS chip. (a) Schematic representation for imposing interstitial flow on VTS chip fabricated with tumor-EC hybrid spheroid, vascular ECs and lymphatic ECs. (b) Confocal images of tumor-EC spheroid with LECs (green; podoplanin) and vascular ECs (red; CD31) under static condition and interstitial flow, respectively. (Scale bars, $400 \mu\text{m}$) (c-e) Comparison of tumor spheroid size (c), blood vessel area (d) and lymphatic vessel area (e) in the VTS chip under static condition and interstitial flow. ($n = 4$) Note that both lymphangiogenesis and angiogenesis were promoted in the VTS chip by application of interstitial flow. All data were expressed as the mean \pm SD. *** $p < 0.001$, n.s. not statistically significant, versus Static. (For interpretation of the references to colour in this figure legend, the reader is referred to the web version of this article.)

4. Discussion

Solid tumors are composed of cancer cells, stromal cells (tumor-associated vascular cells, fibroblasts and immune cells) and ECM components (collagen and fibrin). These factors in combination create a highly interactive 3D microenvironment characterized by cell–cell and cell-ECM interactions as well as local gradients of nutrients, growth factors, and oxygen. Furthermore, the TME plays a major role in the process of tumor survival, such as growth, angiogenesis and drug resistance [53]. Hence, a tumor spheroid resembling a small tumor mass in its morphology and growth kinetics that also has a stromal microenvironment that interacts with the tumor spheroid, representative of the vasculature, should be considered for precise modeling of the 3D TME.

The onset of tumor angiogenesis has been explained as the result of an “angiogenic switch”, which is the transition in the angiogenic balance [54]. During cancer dormancy, antiangiogenic factors are predominantly expressed to prevent tumor outgrowth. However, as tumors grow, the expression of proangiogenic factors is elevated by several stimuli, such as hypoxia. Eventually, the prevalence of proangiogenic factors facilitates the progression of dormant avascular hyperplasia into hypervascularized tumors. Therefore, tumor angiogenesis is inevitable for tumor progression. Therefore, we attempted to develop an aggressive TME model with tumor vascularization. There are two ways to develop intratumoral vessels to feed a tumor: i) the surrounding vessels can be extended toward and penetrate the tumor mass, or ii) vasculogenic mimicry in which the tumor forms blood-carrying channels within the tumor mass, and then, the vessels surrounding the tumor interconnect with the internal channels [40]. In this context, we first established tumor-EC hybrid spheroids by coculturing HepG2 cells and ECs at a 1:1 ratio to recapitulate tumors with intratumoral vasculature. The tumor-EC hybrid spheroids exhibited special features, including sphericity, aggressiveness and angiogenesis potential, compared to tumor spheroids cultured without ECs. In particular, the spherical morphology of the 1:1 hybrid spheroid provided ease of experimentation and highly reproducible results. During tumor intravasation, cancer cells interact with ECs in both a juxtacrine and paracrine manner. Thus, it is worthwhile to analyze how tumor cells affect ECs, either directly or indirectly. Particularly, RNA sequencing of the hybrid spheroids allowed us to understand the transcriptional changes after reconstructing intratumoral vessels within the spheroids. Via enrichment analysis (GO analysis, GSEA, and KEGG), a significant upregulation of the genes related to cell migration and downregulation of genes related to the p53 signaling pathway was identified in the 1:1 hybrid spheroids. Specifically, the overexpression of Vimentin encoded by *VIM* has been reported to be deeply linked to hepatocellular carcinoma metastasis [41]. It has also been reported that the drastic increase of *H19*, a long non-coding RNA, was observed in hepatocellular carcinoma patients and associated with poor prognosis according to the clinical report [42]. Of note, *LAMB3* has been reported to mediate the progression and metastasis of various cancer cells by regulating PI3K/AKT signaling pathway [43] as well as its downstream genes including *ITGA3*, *CCND2*, and *TP53* [55]. These transcriptomic profiles were also in accordance with the protein phenotypes, such as downregulation of p53 tumor suppressor and the induction of the EMT. Moreover, we also identified that vascular gene set, including *PECAM1*, *VWF* and *FLT1*, was enriched in the 1:1 hybrid spheroids, which may be attributed to not only increased population of ECs within the hybrid spheroid but also enhanced pro-angiogenic features of cancer cells. These results implied that the interactions between cancer cells and ECs are required for the modeling of aggressive solid tumors *in vitro*.

Another main challenge of conventional tumor spheroid models is the lack of vasculature adjacent to the tumor spheroid [56].

Through microengineering, we successfully incorporated tumor-EC hybrid spheroids with peritumoral vasculature at the chip level. Introduced ECs were self-assembled into the vascular network, forming perfusable structures, which were interconnected with the tumor spheroid. Thus, our VTS chip allowed us to investigate the interaction between the surrounding vasculature and the tumor spheroid. Interestingly, tumor angiogenesis was promoted by tumor-EC hybrid spheroids compared to cancer-only spheroids. In addition, the results obtained from qRT-PCR revealed that the reciprocal influences between tumor cells and ECs altered the expression of molecular factors that drive angiogenesis. Therefore, we proved that multicellular hybrid spheroids allowed more relevant modeling of the aggressive tumor environment than those comprising cancer cells only. This model can be advantageous for drug screening since cancer aggressiveness is an important determinant of the clinical efficacy of anticancer therapies. One characteristic of tumor vessels is a defective and leaky endothelium that is disorganized, contains focal intercellular openings and has a loose vascular basement membrane [57]. To our best knowledge, there was no attempt to visualize and quantitatively demonstrate FIOs in a vascularized tumor model. Considering that permeable vasculature is a key survival mechanism of tumors by enabling tumor extravasation and limiting the efficacy of drug delivery [47], the development of tumor-associated vasculature is indispensable to reenact the conditions that approximate the pathological TME as closely as possible. In this current manuscript, we successfully demonstrated an increased number of FIOs of vasculature and permeability of blood vessels in adjunction to tumor-EC hybrid spheroid.

Notably, a 3D TME model that retains lymphatic vessels with the blood vessels around the tumor spheroid has not been developed thus far. Here, we generated sophisticated lymphatic and vascular networks on a VTS chip by applying interstitial flow. The phenotype obtained was similar to that in a previous study demonstrating that interstitial flow promoted tumor lymphangiogenesis [52].

Recently, an increasing number of anticancer drug candidates have been advanced through preclinical and clinical development [49]. In this regard, our VTS model showing an aggressive phenotype of cancer with tumor-associated vasculature can be a valuable *in vitro* tool for validating the effects of drugs on tumor tissues, including cancer cell death. In this study, we demonstrated that a high dose (10 nM) of axitinib, an anticancer drug targeting angiogenesis [58], caused a remarkable regression of both tumor spheroid growth and blood vessel volume on the VTS chip. However, when axitinib was administered at an early stage, before vascularization, the size reduction in the tumor spheroid was not observed, despite dose-dependent inhibition of angiogenesis [59, 60]. These results imply that the tumor-associated vasculature is closely associated with the delivery and efficacy of axitinib; hence, tumor vascularization is necessary to recapitulate tumor progression and growth.

However, there was also a limitation to analyze the phenomena on VTS chips in a 3D context due to physical constraints imposed by light scattering during 3D imaging. To overcome this issue, we additionally suggested the on-chip CUBIC tissue clearing protocols to clearly obtain 3D in-depth confocal images of our VTS chips (Supplementary Fig. S7a,b). Notably, the clear on-chip spheroid conditions allowed accurate 3D signal visualization and quantification of the VTS (Supplementary Fig. S7c–g and Supplementary Video S1). As there was no attempt to on-chip clearing with fully vascularized tumor spheroid, it might be widely exploited in the fields of 3D imaging of microfluidic chip devices.

In summary, our VTS model simulated some of the complexity of *in vivo* tumors, including the 3D spheroid structure with intra-

tumoral microvessels, interconnected blood vessels with increased permeability around the tumor, a lymphatic vessel network, stromal fibroblasts and the ECM. By extension, the VTS model introduced with patient-derived multicellular tumor spheroids and cancer-associated fibroblasts, instead of HepG2 cells and lung fibroblasts, respectively, may be a bridge between *in vitro* cultured tumor cells and *in vivo* pathological conditions, to promote clinical applications in personalized medicine. Yet, our current model has some challenges. For instance, owing to the irregular and flat morphology, HepG2-only spheroids might not be exposed to hypoxic conditions that are associated with pathological features of solid tumors. Thus, application of additional tumor-specific environments, including hypoxic conditions, to VTS chips may overcome the limitation of our spheroids, such as not displaying layered structures of multicellular tumor spheroids as previously reported [61]. In addition, the immune milieu associated with tumors can be reconstituted by coculturing immune cells on the chip to facilitate the advanced modeling of the pathological tumor environment. Moreover, it is worthwhile to further investigate intravasation and extravasation of cancer cells for metastasis on our VTS chip as tumor-EC hybrid spheroids exhibit aggressive and metastatic phenotypes. Considering that our VTS chip could not completely verify the perfusion of reconstituted lymphatic vessels, future studies regarding the reconstitution of perfusable lymphatic vessels in the vascularized tumor chips would be valuable to understand cancer metastasis since the lymphatic system is a primary mechanism for tumors to move, or metastasize to distant organs [51].

5. Conclusion

We engineered an *in vitro* 3D vascularized tumor spheroid model exhibiting pathologically relevant features. We first generated a tumor-EC hybrid spheroid with varying cancer cell to EC ratios. We found that 1:1 hybrid spheroids showed more spherical morphology and high aggressiveness due to interactions between cancer cells and ECs. Then, we fabricated a VTS chip with tumor-EC hybrid spheroids. Our VTS model also recapitulated fenestrated blood vessels, a hallmark of leaky tumor vasculature. We also demonstrated the effects of axitinib on tumor spheroids and tumor-associated angiogenesis depending on varying doses and exposure times. Finally, we engineered a complicated TME using both lymphatic and blood vessels within the VTS chip. Thus, the established VTS chip could serve as a valuable proof-of-concept for drug efficacy testing platforms.

Declaration of Competing Interest

The authors declare that they have no known competing financial interests or personal relationships that could have appeared to influence the work reported in this paper.

The authors declare no conflict of interest.

CRediT authorship contribution statement

Jungho Ahn: Conceptualization, Formal analysis, Investigation, Writing – review & editing. **Da-Hyun Kim:** Conceptualization, Formal analysis, Investigation, Writing – review & editing. **Dong-Jun Koo:** Conceptualization, Formal analysis, Investigation. **Jungeun Lim:** Investigation. **Tae-Eun Park:** Validation. **Jungseub Lee:** Investigation. **Jihoon Ko:** Investigation. **Seongchan Kim:** Investigation. **Minjae Kim:** Investigation. **Kyung-Sun Kang:** Validation. **Dal-Hee Min:** Validation. **Sung-Yon Kim:** Validation. **YongTae Kim:** Validation. **Noo Li Jeon:** Validation.

Acknowledgements

This work was supported by the National Research Foundation of Korea (NRF) grant funded by the Korea government (MSIT) (Nos. 2021R1C1C2010636 and 2021R1A3B1077481).

Supplementary materials

Supplementary material associated with this article can be found, in the online version, at doi:10.1016/j.actbio.2022.10.009.

References

- [1] H. Luo, G. Tu, Z. Liu, M. Liu, Cancer-associated fibroblasts: a multifaceted driver of breast cancer progression, *Cancer Lett.* 361 (2) (2015) 155–163.
- [2] J. Ahn, Y.J. Sei, N.L. Jeon, Y. Kim, Tumor microenvironment on a chip: the progress and future perspective, *Bioengineering* 4 (3) (2017) 64.
- [3] J. Ahn, J. Ko, S. Lee, J. Yu, Y. Kim, N.L.J. Jeon, Microfluidics in nanoparticle drug delivery; from synthesis to pre-clinical screening, *Adv. Drug Deliv. Rev.* 128 (2018) 29–53.
- [4] S. Thakkar, D. Sharma, K. Kalia, R.K. Tekade, Tumor microenvironment targeted nanotherapeutics for cancer therapy and diagnosis: a review, *Acta Biomater.* 101 (2020) 43–68.
- [5] S. Koontongkaew, The tumor microenvironment contribution to development, growth, invasion and metastasis of head and neck squamous cell carcinomas, *J. Cancer* 4 (1) (2013) 66.
- [6] D. Hanahan, R.A. Weinberg, Hallmarks of cancer: the next generation, *Cell* 144 (5) (2011) 646–674.
- [7] H.F. Tsai, A. Trubelja, A.Q. Shen, G. Bao, Tumour-on-a-chip: microfluidic models of tumour morphology, growth and microenvironment, *J. R. Soc. Interface* 14 (131) (2017) 20170137.
- [8] L. Eklund, M. Bry, K. Alitalo, Mouse models for studying angiogenesis and lymphangiogenesis in cancer, *Mol. Oncol.* 7 (2) (2013) 259–282.
- [9] I.K. Zervantonakis, S.K. Hughes-Alford, J.L. Charest, J.S. Condeelis, F.B. Gertler, R.D. Kamm, Three-dimensional microfluidic model for tumor cell intravasation and endothelial barrier function, *Proc. Natl. Acad. Sci. U. S. A.* 109 (34) (2012) 13515–13520.
- [10] J.S. Jeon, S. Bersini, M. Gilardi, G. Dubini, J.L. Charest, M. Moretti, R.D. Kamm, Human 3D vascularized organotypic microfluidic assays to study breast cancer cell extravasation, *Proc. Natl. Acad. Sci. U. S. A.* 112 (1) (2015) 214–219.
- [11] J. Ahn, J. Lim, N. Jusoh, J. Lee, T.E. Park, Y. Kim, J. Kim, N.L. Jeon, Biotechnology, 3D microfluidic bone tumor microenvironment comprised of hydroxyapatite/fibrin composite, *Front. Bioeng. Biotechnol.* 7 (2019) 168.
- [12] M. Chung, J. Ahn, K. Son, S. Kim, N.L. Jeon, Biomimetic model of tumor microenvironment on microfluidic platform, *Adv. Healthc. Mater.* 6 (15) (2017) 1700196.
- [13] A. Nishiguchi, M. Matsusaki, M.R. Kano, H. Nishihara, D. Okano, Y. Asano, H. Shimoda, S. Kishimoto, S. Iwai, M. Akashi, *In vitro* 3D blood/lymph-vascularized human stromal tissues for preclinical assays of cancer metastasis, *Biomaterials* 179 (2018) 144–155.
- [14] J. Ko, J. Ahn, S. Kim, Y. Lee, J. Lee, D. Park, N.L. Jeon, Tumor spheroid-on-a-chip: a standardized microfluidic culture platform for investigating tumor angiogenesis, *Lab Chip* 19 (17) (2019) 2822–2833.
- [15] J. Kim, H. Park, H. Kim, Y. Kim, H.J. Oh, S. Chung, Microfluidic one-directional interstitial flow generation from cancer to cancer associated fibroblast, *Acta Biomater.* 144 (2022) 258–265.
- [16] S.Y. Jeong, J.H. Lee, Y. Shin, S. Chung, H.J. Kuh, Co-culture of tumor spheroids and fibroblasts in a collagen matrix-incorporated microfluidic chip mimics reciprocal activation in solid tumor microenvironment, *PLoS One* 11 (7) (2016) e0159013.
- [17] H.G. Yi, Y.H. Jeong, Y. Kim, Y.J. Choi, H.E. Moon, S.H. Park, K.S. Kang, M. Bae, J. Jang, H. Youn, A bioprinted human-glioblastoma-on-a-chip for the identification of patient-specific responses to chemoradiotherapy, *Nat. Biomed. Eng.* 3 (7) (2019) 509–519.
- [18] V. Surendran, D. Rutledge, R. Colmon, A. Chandrasekaran, A novel tumor-immune microenvironment (TIME)-on-Chip mimics three dimensional neutrophil-tumor dynamics and neutrophil extracellular traps (NETs)-mediated collective tumor invasion, *Biofabrication* 13 (3) (2021) 035029.
- [19] J. Song, H. Choi, S.K. Koh, D. Park, J. Yu, H. Kang, Y. Kim, D. Cho, N.L. Jeon, High-throughput 3D *in vitro* tumor vasculature model for real-time monitoring of immune cell infiltration and cytotoxicity, *Front. Immunol.* (12) (2021) 733317.
- [20] S. Lee, H. Kang, D. Park, J. Yu, S.K. Koh, D. Cho, D.H. Kim, K.S. Kang, N.L. Jeon, Modeling 3D human tumor lymphatic vessel network using high-throughput platform, *Adv. Biol.* 5 (2) (2021) 2000195.
- [21] Y. Lee, J.W. Choi, J. Yu, D. Park, J. Ha, K. Son, S. Lee, M. Chung, H.Y. Kim, N.L. Jeon, Microfluidics within a well: an injection-molded plastic array 3D culture platform, *Lab Chip* 18 (16) (2018) 2433–2440.
- [22] I.B. Fridman, J. Kostas, M. Gregus, S. Ray, M.R. Sullivan, A.R. Ivanov, S. Cohen, T. Konry, High-throughput microfluidic 3D biomimetic model enabling quantitative description of the human breast tumor microenvironment, *Acta Biomater.* 132 (2021) 473–488.

- [23] F. Hirschhaeuser, H. Menne, C. Dittfeld, J. West, W. Mueller-Klieser, L.A. Kunz-Schughart, Multicellular tumor spheroids: an underestimated tool is catching up again, *J. Biotechnol.* 148 (1) (2010) 3–15.
- [24] K. Carver, X. Ming, R.L. Juliano, Multicellular tumor spheroids as a model for assessing delivery of oligonucleotides in three dimensions, *Mol. Ther. Nucleic Acids* 3 (2014) e153.
- [25] K. Moshksayyan, N. Kashaninejad, M.E. Warkiani, J.G. Lock, H. Moghadas, B. Firoozabadi, M.S. Saidi, N.T. Nguyen, Spheroids-on-a-chip: recent advances and design considerations in microfluidic platforms for spheroid formation and culture, *Sens. Actuators B: Chem.* 263 (2018) 151–176.
- [26] B.W. Huang, J.Q. Gao, Application of 3D cultured multicellular spheroid tumor models in tumor-targeted drug delivery system research, *J. Control Release* 270 (2018) 246–259.
- [27] Y. Nashimoto, R. Okada, S. Hanada, Y. Arima, K. Nishiyama, T. Miura, R. Yokokawa, Vascularized cancer on a chip: the effect of perfusion on growth and drug delivery of tumor spheroid, *Biomaterials* 229 (2020) 119547.
- [28] H. Shoval, A. Karsch-Bluman, Y. Brill-Karniely, T. Stern, G. Zamir, A. Hubert, O. Benny, Tumor cells and their crosstalk with endothelial cells in 3D spheroids, *Sci. Rep.* 7 (1) (2017) 1–11.
- [29] A. Sobrino, D.T. Phan, R. Datta, X. Wang, S.J. Hachey, M. Romero-López, E. Gratton, A.P. Lee, S.C. George, C.C. Hughes, 3D microtumors in vitro supported by perfused vascular networks, *Sci. Rep.* 6 (1) (2016) 1–11.
- [30] J. Song, A. Miermont, C.T. Lim, R.D. Kamm, A 3D microvascular network model to study the impact of hypoxia on the extravasation potential of breast cell lines, *Sci. Rep.* 8 (1) (2018) 1–11.
- [31] M.G. Kellermann, L.M. Sobral, S.D. da Silva, K.G. Zecchin, E. Graner, M.A. Lopes, L.P. Kowalski, R.D. Coletta, Mutual paracrine effects of oral squamous cell carcinoma cells and normal oral fibroblasts: induction of fibroblast to myofibroblast transdifferentiation and modulation of tumor cell proliferation, *Oral Oncol.* 44 (5) (2008) 509–517.
- [32] J. Folkman, in: *Role of Angiogenesis in Tumor Growth and Metastasis*, Seminars in Oncology, Elsevier, 2002, pp. 15–18.
- [33] S.W. Lee, H.S. Kwak, M.H. Kang, Y.Y. Park, G.S. Jeong, Fibroblast-associated tumor microenvironment induces vascular structure-networked tumouroid, *Sci. Rep.* 8 (1) (2018) 1–12.
- [34] Z. Hu, Y. Cao, E.A. Galan, L. Hao, H. Zhao, J. Tang, G. Sang, H. Wang, B. Xu, S. Ma, Vascularized tumor spheroid-on-a-chip model verifies synergistic vasoprotective and chemotherapeutic effects, *ACS Biomater. Sci. Eng.* 8 (3) (2022) 1215–1225.
- [35] S.M. Ehsan, K.M. Welch-Reardon, M.L. Waterman, C.C. Hughes, S.C. George, A three-dimensional in vitro model of tumor cell intravasation, *Integr. Biol.* 6 (6) (2014) 603–610.
- [36] S. Lee, S. Kim, D.J. Koo, J. Yu, H. Cho, H. Lee, J.M. Song, S.Y. Kim, D.H. Min, N.L. Jeon, 3D microfluidic platform and tumor vascular mapping for evaluating anti-angiogenic RNAi-based nanomedicine, *ACS Nano* 15 (1) (2020) 338–350.
- [37] H. Lee, S. Kim, M. Chung, J.H. Kim, N.L. Jeon, A bioengineered array of 3D microvessels for vascular permeability assay, *Microvasc. Res.* 91 (2014) 90–98.
- [38] E.A. Susaki, H.R. Ueda, Whole-body and whole-organ clearing and imaging techniques with single-cell resolution: toward organism-level systems biology in mammals, *Cell Chem. Biol.* 23 (1) (2016) 137–157.
- [39] J. Folkman, Tumor angiogenesis factor, *Adv. Cancer Res.* 34 (8) (1974) 2109–2113.
- [40] R. Folberg, M.J. Hendrix, A.J. Maniotis, Vasculogenic mimicry and tumor angiogenesis, *Am. J. Pathol.* 156 (2) (2000) 361–381.
- [41] L. Hu, S.H. Lau, C.H. Tzang, J.M. Wen, W. Wang, D. Xie, M. Huang, Y. Wang, M.C. Wu, J. Huang, Association of vimentin overexpression and hepatocellular carcinoma metastasis, *Oncogene* 23 (1) (2004) 298–302.
- [42] Á. Rojas, A. Gil-Gómez, P. de la Cruz-Ojeda, R. Muñoz-Hernández, Y. Sánchez-Torrijos, R. Gallego-Durán, R. Millán, M.C. Rico, R. Montero-Vallejo, S. Gato-Zambrano, Long non-coding RNA H19 as a biomarker for hepatocellular carcinoma, *Liver Int.* 42 (6) (2022) 1410–1422.
- [43] H. Zhang, Y.Z. Pan, M. Cheung, M. Cao, C. Yu, L. Chen, L. Zhan, Z.W. He, C.Y. Sun, Disease, LAMB3 mediates apoptotic, proliferative, invasive, and metastatic behaviors in pancreatic cancer by regulating the PI3K/Akt signaling pathway, *Cell Death Dis.* 10 (3) (2019) 1–14.
- [44] Y. Lei, W. Yan, Z. Lin, J. Liu, D. Tian, P. Han, Comprehensive analysis of partial epithelial mesenchymal transition-related genes in hepatocellular carcinoma, *J. Cell Mol. Med.* 25 (1) (2021) 448–462.
- [45] C. Dong, J. Zhang, S. Fang, F. Liu, IGFBP5 increases cell invasion and inhibits cell proliferation by EMT and Akt signaling pathway in Glioblastoma multiforme cells, *Cell Div.* 15 (1) (2020) 1–9.
- [46] G. Giannelli, P. Koudelkova, F. Diturì, W. Mikulits, Role of epithelial to mesenchymal transition in hepatocellular carcinoma, *J. Hepatol.* 65 (4) (2016) 798–808.
- [47] S. Azzi, J.K. Hebda, J. Gavard, Vascular permeability and drug delivery in cancers, *Front. Oncol.* 3 (2013) 211.
- [48] H. Hashizume, P. Baluk, S. Morikawa, J.W. McLean, G. Thurston, S. Roberge, R.K. Jain, D.M. McDonald, Openings between defective endothelial cells explain tumor vessel leakiness, *Am. J. Pathol.* 156 (4) (2000) 1363–1380.
- [49] B. Zhang, X. Zhang, T. Zhou, J. Liu, Therapy, Clinical observation of liver cancer patients treated with axitinib and cabozantinib after failed sorafenib treatment: a case report and literature review, *Cancer. Biol. Ther.* 16 (2) (2015) 215–218.
- [50] S.A. Stacker, S.P. Williams, T. Karnezis, R. Shayan, S.B. Fox, M.G. Achen, Lymphangiogenesis and lymphatic vessel remodelling in cancer, *Nat. Rev. Cancer* 14 (3) (2014) 159–172.
- [51] L.C. Dieterich, M. Detmar, Tumor lymphangiogenesis and new drug development, *Adv. Drug Deliv. Rev.* 99 (2016) 148–160.
- [52] Y. Cho, K. Na, Y. Jun, J. Won, J.H. Yang, S. Chung, Three-dimensional in vitro lymphangiogenesis model in tumor microenvironment, *Front. Bioeng. Biotechnol.* (2021) 826.
- [53] M. Wang, J. Zhao, L. Zhang, F. Wei, Y. Lian, Y. Wu, Z. Gong, S. Zhang, J. Zhou, K. Cao, Role of tumor microenvironment in tumorigenesis, *J. Cancer* 8 (5) (2017) 761.
- [54] G. Bergers, L.E. Benjamin, Tumorigenesis and the angiogenic switch, *Nat. Rev. Cancer* 3 (6) (2003) 401–410.
- [55] J. Hou, L. Wang, D. Wu, The root of Actinidia chinensis inhibits hepatocellular carcinomas cells through LAMB3, *Cell Biol. Toxicol.* 34 (4) (2018) 321–332.
- [56] S. Nath, G.R. Devi, Three-dimensional culture systems in cancer research: Focus on tumor spheroid model, *Pharmacol. Ther.* 163 (2016) 94–108.
- [57] D.M. McDonald, P. Baluk, Significance of Blood Vessel Leakiness in Cancer, *AACR*, 2002.
- [58] T.K. Choueiri, Axitinib, a novel anti-angiogenic drug with promising activity in various solid tumors, *Curr. Opin. Investig. Drugs* 9 (6) (2008) 658–671.
- [59] X.H. Zhang, E.Q. Qiao, Z. Gao, H.Q. Yuan, P.F. Cai, X.M. Li, Y.H. Gu, Efficacy of combined axitinib with dacarbazine in a B16F1 melanoma xenograft model, *Oncol. Lett.* 6 (1) (2013) 69–74.
- [60] D.D. Hu-Lowe, H.Y. Zou, M.L. Grazzini, M.E. Hallin, G.R. Wickman, K. Amundson, J.H. Chen, D.A. Rewolinski, S. Yamazaki, E.Y. Wu, Nonclinical antiangiogenesis and antitumor activities of axitinib (AG-013736), an oral, potent, and selective inhibitor of vascular endothelial growth factor receptor tyrosine kinases 1, 2, 3, *Clin. Cancer Res.* 14 (22) (2008) 7272–7283.
- [61] R.M. Sutherland, Cell and environment interactions in tumor microregions: the multicell spheroid model, *Science* 240 (4849) (1988) 177–184.